Methodologies for Landing Autonomous Aerial Vehicles on Maritime Vessels

Shadi Abujoub, Johanna McPhee, Rishad A. Irani*

[a] *Multi-Domain Laboratory, Department of Mechanical and Aerospace Engineering, Carleton University, Ottawa, Ontario, K1S 5B6, Canada*

Abstract

One of the key challenges to the safe operation of UAVs at sea is the relative motion that exists between the UAV and ship during landing. The scope of this work is the development and evaluation of methodologies for improving UAV landing performance. The new methodologies are known as the Signal Prediction Algorithm (SPA), Active Heave Compensation (AHC) and the Landing Period Indicator (LPI). To promote interoperability, the methodologies do not require any specific ship equipment.

To evaluate the methodologies on an existing comprehensive UAV model, ShipMo3D was used to generate 105 sets of ship motion in sea states 2–6, headings 0–180° and speeds 6–10 knots. Within the simulation the UAV, equipped with a Light Detection and Ranging (LIDAR) system, measures the ship motion *in situ*. Using the Signal Prediction Algorithm (SPA), the UAV forecasts the ship motion and potential landing opportunities. The UAV can also use the SPA and the AHC system to maintain a safe hover position above the ship deck and determine landing trajectories with a specific touchdown velocity. The UAV can also employ the novel Landing Period Indicator (LPI) system which calculates an estimate of the ship's energy and determines opportune times for safe landings.

The results indicate that the methodologies can improve the landing performance of autonomous helicopters. For the 105 sets of ship motion, using the

combination of the SPA, AHC, and LPI improved landing success by up to 34% when compared to a common landing controller.

Keywords: UAV, Uninhabited Aerial Vehicles, Autonomous Systems, Signal Prediction, Maritime Operations, Ship Motion, Energy Index, Landing Period Indicator, Aircraft Landing Systems, Interoperability

1. Introduction

The use of small Uninhabited Aerial Vehicles (UAVs) for maritime operations include oceanographic data collection [1], search and rescue [2], and wildlife monitoring [3]. Due to the limited range of most UAVs, and the 'at-sea' nature of maritime missions, it is necessary to recover the UAV on the deck of a marine vessel. Fig. 1 illustrates the relative motions and frames of the two crafts. Additionally, the figure shows the four phases of landing a rotorcraft [4, 5]: tracking, high hover, low hover and final descent. The tracking/homing phase is where the UAV approaches the ship at its cruising altitude and once it is within proximity to the ship, the UAV reduces its altitude to the high hover to begin landing. The high hover phase is where the UAV is at a stand-off clear of the ship's structures and final preparations are made for landing. Once cleared to land, the UAV then descends to a low hover; when at the low hover stand-off, the UAV can commence the final landing on the deck of the ship.

During the general UAV flight and tracking phases, flight control systems [6] and navigation and control techniques [7] are well studied. However, the final descent and landings "...on moving platforms is still an unsolved problem due to

*Corresponding author
Email addresses: ShadiAbujoub@cmail.carleton.ca (Shadi Abujoub), JohannaMcPhee3@cmail.carleton.ca (Johanna McPhee), Rishad.Irani@carleton.ca (Rishad A. Irani)

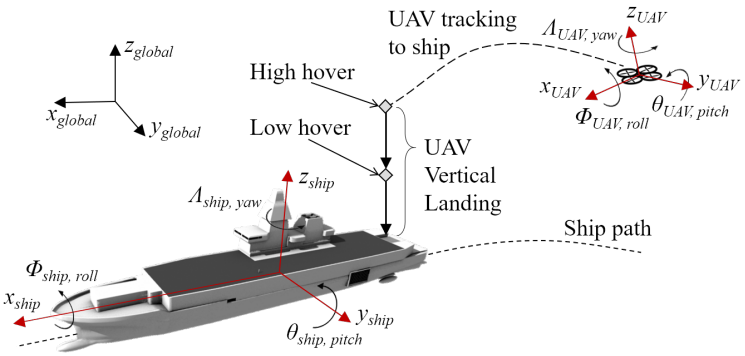

Figure 1: Recovery phases of a UAV tracking, high hover, low hover and final descent. The various coordinate frames and motions are also illustrated.

the inherent difficulties of operation in this kind of scenario" [8]. The current work focuses on methods to improve safe landings on a moving vessel at sea.

During the landing manoeuvre, there are uncoupled and relative motions between the two independent bodies, aircraft and ship, which causes a great challenge. Best practices and safety guidelines for shipboard landing operations state threshold ship pitch and roll limits [4, 5]. In addition to the guidelines for conventional rotorcraft, a human pilot's training, experience and intuition account for the relative motion. Autonomous UAVs must be able to determine when to begin, abort and adjust a landing attempt as a pilot would. Ships capable of supporting rotorcraft vehicles may employ secondary hardware such as positioning beacons, transmitters and receivers to facilitate UAVs with landing. The need to limit the required deck hardware is desirable as it promotes cross-platform capability, interoperability [9], between UAVs and ships without specialised hardware or systems.

The trend to land UAVs are with the aid of vision systems[10, 11, 12, 13, 14, 15, 16, 17, 18] or tethered systems [8, 19, 20, 21, 22]. With respect to interoperability, a potential limiting factor of vision systems is that they often require

specific geometry, objects or markers on the ship [18]. Additionally, vision systems often require a supplementary system when operating in the night, fog or other inclement weather conditions [23]. To alleviate some of the risk during heavy weather, tethered systems could be used. However, tethers generally require specialised ship hardware [22] and could limit interoperability.

The current work proposes three new landing methodologies for autonomous UAVs to land on a moving vessel without additional ship hardware, ground crew, a tether or a vision system; thus promoting interoperability. In the current work, all of required sensory equipment is aboard the UAV. The methods address the final descent of the UAV, while other techniques [6, 7] could be used for flight dynamics, tracking and homing of the UAV's mission. The new methodologies can be used in conjunction with each other to enhance the performance and reliability. The proposed methods are tested within simulation using a small autonomous quadcopter UAV and, as a benchmark, compared against a basic controller for landing. The methods are independent of the specific UAV and can be applied to various vertical landing aircrafts. The flight controllers are linear Proportional-Integral-Derivative controllers as they "have shown adequate performance" [7].

The presented work provides a basis of laboratory and scale testing of the new landing methodologies. As the current work is simulation based it is difficult to emulate and provide a comparison to defacto vision systems and a comparison could lead to misinterpretations. It has been mentioned that ship landings are an "unsolved problem" [8] so is unwise to make "state-of-the-art" claims to other marine landing methods for a comparison study. Therefore, to compare and contrast the current work, a simple feedback landing system is used which other researchers can use as a benchmark.

In the following section a summary of past related work is presented. The details of the new proposed landing methodologies are described in Section 3.

Additionally, within Section 3 there is a small comparative discussion of their relative performance. Section 4 presents the results of a case study performed in simulation and the methodologies are ranked and show an improvement when compared to the benchmark feedback landing system. The paper concludes with some final remarks and future avenues of work.

2. Background

Many researchers have examined various aspects of the ship tracking and landing process of UAVs. Focusing on ship tracking, Arora et al. [14] found success by using Light Detection and Ranging (LIDAR) and camera based control to track a helicopter to a ship without secondary deck mounted infrastructure; however, the landing deck geometry and markings are known. Sanchez et al. [13] suggest that using a downward facing camera with a state estimator could be used to track ship motion for autonomous landing. Oh et al. [20, 21] propose using a tether between a helicopter and ship to assist with landing; however, unlike the Recovery, Assist, Secure and Traverse (RAST) system [22], the tether angle would be used to find the relative orientation between the helicopter and ship to facilitate the ship deck tracking.

Not focusing on landing specifically, Razmi and Afshinfar [24] developed a neural network based control system for position and attitude tracking control of a UAV. Focusing on the landing, Garratt and Anavatti [25] used a neural network controller to produce heave trajectories for a UAV. Similarly, Moriarty et al. [16] suggest using a stereo camera to track a ship's landing zone and a neural network to predict opportune landing windows. Hervas et al. [26] developed a landing control algorithm for unmanned vehicles on moving platforms that controlled the landing based solely on the relative heave motion between UAV and ship deck. While their simulations showed the algorithm was effective, the algorithm did not

discriminate between safe landing times nor provide a method for tracking the ship trajectory. Ngo and Sultan [27] presented a model predictive control (MPC) design for helicopter shipboard operations in the presence of ship air wakes and rough seas. While the MPC method proved to be feasible in simulations, the researchers did not address the issue of the compatibility of their control method to other helicopter-ship combinations other than that which was simulated. Xia et al. [28] proposed a mission planning technique that focuses on the approaching and landing stage. In their simulation results, the UAV lands near or close to the centre-of-gravity where the roll and pitch motions are minimal, while in practice most landings occur at the aft of a marine vessel. Additionally, their simulations assume that the UAV has access to the ship's motion information through a direct communication and measurement system, which could be a hinderance to interoperability. Huang et al. [29] developed a fixed-time landing controller, which was examined within simulation for a sea state 2 and 6. Their simulation work did yield promising results; however, the work did not provide insight into appropriate landing opportunities as for their work the ship motions reported primarily fell within the common safe operating limits [4, 5].

Examining ship motion, Ferrier et al. [30] used an Energy Index (EI) to predict quiescent periods of a vessel's motion such that

$$EI = a_1\dot{w}^2 + a_2\ddot{w}^2 + a_3\dot{j}^2 + a_4\ddot{j}^2 + a_5\dot{p}^2 + a_6\ddot{p}^2 + a_7\dot{q}^2 + a_8\ddot{q}^2, \tag{1}$$

where a_i are weighted dynamic coefficients, w is heave, j is sway, p is roll, and q is pitch, while the dot notation indicate the first and second time derivatives. Ferrier et al. [30] state that the dynamic coefficients are tuned based on the "aircraft limitation scale" and ship motion parameters. Ferrier et al. [30] claim good agreement between their predicted energy and ship motion; however, it is

unclear to the current authors how they established their dynamic coefficients. Furthermore, their energy index only considers the cumulative motion of the ship and does not consider if the ship is within safe thresholds. Based on Ferrier et al.'s work, a new Landing Period Indicator (LPI) is proposed in the current work that is independent of vessel and aircraft type without *a priori* ship or UAV coefficients.

Fourie [31] used a Global Positioning System (GPS) for the autonomous landing of a remote control helicopter on a towed moving platform. Fourie's work was part of a larger initiative to predict ship energy [32]. Fourie comments on the need to investigate and gauge the performance of landing systems and quantify when they should be used.

As a contribution to the field, the current work proposes landing methodologies for an infrastructure free, non-vehicle specific system that facilitates the autonomous determination of safe landing times while also compensating for the relative motion between the UAV and ship. To implement the methods, one must be able to measure or estimate the motions of the ship or the relative motions that exist between the UAV and the ship.

Forecasting ship motion accurately *in situ* can serve to improve daily maritime activities such as active ship stability, cargo transfer, fire accuracy of weapon systems, and the interfacing of aerial and ocean vehicles [33]. Despite the nonlinearity of ship motion, linear methods of forecasting, such as Auto Regressive (AR) [34] and Auto Regressive Moving Average (ARMA) [35], have been used to predict ship motion. Zhao et al. [36] investigated using a Minor Component Analysis (MCA) prediction algorithm to predict ship motion that outperformed Neural Networks (NN) and an Auto Regressive (AR) model. For a 5 second prediction, the NN and AR respectively required 3.4 and 1.6 seconds of computational time on a 1.6 GHz PC, compared to the 0.1 seconds of the MCA. The added computational time for NN and AR raises questions of the feasibility of implementing

such systems for online estimation.

Chung et al. [37] used a Kalman filter to estimate ship motion online using estimated wave-excitation data as an input. The researchers estimated the wave-excitation information based on measured ship motion and used the ship's response amplitude operators (RAOs) to extrapolate future ship motion information. However, relying on knowledge of the ship's response function could limit the interoperability. Zhen et al. [38] used a particle filter theory to estimate ship deck motion for a fixed wing UAV landing system. The presented results, indicate that the heave estimate could have an 0.5 m error in "smooth" sea conditions, and up to 5 m error in "severe" conditions. For Zhen et al.'s work the errors where suitable for their compensation of a fixed-wing UAV landing. A signal prediction independent of vessel type was used for active heave compensation winches, allowing the system to actively pay-in or reel-out line to the towed object to reduce transmitted motion of subsurface equipment [39]. It is hypothesized that a similar Signal Prediction Algorithm (SPA) [39, 40, 41] may be used on-board a UAV to facilitate landing within specified motion thresholds and improve landing efficiency by decreasing the number of landing attempts. The SPA system has been shown to predicted a mean angular error of 0.29, 0.89 and 1.41 deg when forecasting the signal 1, 3 and 10 seconds respectively [40]. Within the current work, it is assumed that the UAV is equipped with a LIDAR measurement system and is able to determine the ship motion [41].

One of the proposed methodologies uses the SPA to search for periods where the ship motion is within specified safe thresholds to land. The SPA methodology is further expanded to use the SPA to improve landing performance by compensating for the relative vertical displacement between the UAV and the ship. The developed system uses the SPA to predict future ship heave positions and preemptively adjusts the UAV's position to a safe static hover height. The altitude adjustment removes the need for the UAV to motion match the ship

deck [42, 23, 28]. Additionally, an Active Heave Compensation (AHC) system is also used to plan trajectories that land the UAV with a specified relative impact velocity.

The proposed Landing Period Indicator (LPI) is an alternative novel method which aims to improve landing performance without the use of signal prediction. The LPI self-tunes system parameters based on the UAV's LIDAR measurements of the relative motion during an initialization hover period above the ship deck. The LPI identifies the signal energy and rate-of-change of energy of the signals from the data collected during initialization from the motions. The LPI system will then attempt to land the UAV when the system energy is low, suggesting decreased relative motion.

A proof-of-concept study is performed to evaluate the landing performance of the SPA, LPI, or AHC for a UAV which measures the ship motion. The study assesses the UAV's ability to land within specified $\pm 5^\circ$ roll and $\pm 2^\circ$ pitch thresholds with an impact velocity less than 1 m/s. The study also analyzes the effects of combining the landing methodologies together and highlights the effectiveness of the systems.

3. Proposed Landing Methodologies

This section outlines the development and implementation of the Signal Prediction Algorithm (SPA), the Landing Period Indicator (LPI) and Active Heave Compensation (AHC) methodologies. The methods are designed in such a way that each method can be used individually or combined.

3.1. Signal Prediction Algorithm (SPA)

A signal prediction algorithm provides a method in which a signal or motion data can be forecasted into the future. The signal prediction is composed of three parts: mode detection, estimation, and prediction. To predict the motion,

the periodic components, the modes, are identified. These modes are found by decomposing the measured signal $s(t)$ into a set of N sine waves expressed as

$$s(t) = \sum_{i=1}^{N} A_i \sin\,(2\pi f_i t + \varphi_i) + v(t), \tag{2}$$

where the amplitude A, frequency f, and phase φ of each mode i is obtained by taking the Fast Fourier Transform (FFT) of past data over a specified time interval and the static signal offset is denoted by $v(t)$. The specified observation window for the FFT, referred to as T_{FFT}, and sampling frequency are chosen such that the lowest frequency of the wave spectrum can be detected, while also preventing aliasing.

As conditions change, the number of modes N and associated frequencies f can change with time; therefore, to predict the periodic motion, a peak detection algorithm is performed at every T_{FFT} interval on the latest set of measured data. The peak detection algorithm determines the amplitude A_{FFT} and frequency f_{FFT} of each mode of the dominant peaks in the FFT spectrum. A peak in the FFT spectrum is said to be dominate when it exceeds a peak detection sensitivity μ which is set by the user. When a new set of modes is identified, it is used to initialize an observer model with a new set of parameters: A_{FFT}, f_{FFT}, φ_{FFT}, and N. From the identified modes, the observer model is given as

$$\begin{aligned} \dot{\mathbf{x}} &= \begin{bmatrix} A_1 & 0 & \dots & \dots & 0 \\ 0 & A_2 & \ddots & & \vdots \\ \vdots & \ddots & \ddots & \ddots & \vdots \\ \vdots & & \ddots & A_N & 0 \\ 0 & \vdots & \vdots & 0 & 0 \end{bmatrix} \begin{bmatrix} x_1 \\ x_2 \\ \vdots \\ x_N \\ x_{off} \end{bmatrix}, \\ s(t) &= \begin{bmatrix} C_1 & C_2 & \cdots & C_N & 1 \end{bmatrix} \mathbf{x}, \end{aligned} \tag{3}$$

where x_{off} is the static offset, and after each T_{FFT} identification interval, A_i is

solved as

$$A_i = \begin{bmatrix} 0 & 1 \\ -(2\pi f_i(t))^2 & 0 \end{bmatrix}. \tag{4}$$

Discretizing the continuous system model in Equation 3 yields for each time step k

$$\mathbf{x}_{k+1} = \exp(\mathbf{A}\Delta T)\mathbf{x}_k \ , \qquad s_k = \mathbf{C}\mathbf{x}_k, \tag{5}$$

where the discrete system matrix $\mathbf{\Psi}$ is represented by the term $\exp(\mathbf{A}\Delta T)$.

The observer model is used to continuously estimate the mode parameters A_{FFT} and φ_{FFT} such that the latest signal measurements are used to adapt A_{FFT} and φ_{FFT} at each time step. For the prediction algorithm, a discrete Kalman filter is implemented to estimate the system states and has the form

$$\hat{x}_{k+1} = \mathbf{\Psi}\hat{\mathbf{x}}_\mathbf{k} + \mathbf{L}(s_k - \hat{s}_k), \qquad \hat{s}_k = \mathbf{C}\hat{\mathbf{x}}_\mathbf{k}, \tag{6}$$

where k is the current time step, $\mathbf{\Psi}$ is the discrete system matrix, $\hat{\mathbf{x}}$ is the vector of observed states, $\mathbf{L}$ is the observer gains matrix, $\hat{s}$ and s are the estimated motion and measured motion respectively, and $\mathbf{C}$ is the system output matrix. The discrete system matrix, observed states and system output matrix were derived following the work of Kuchler et al. [3] and the observer gain matrix is found by the solution to the discrete algebraic Riccati equation.

From each detected mode, two observer states $x_{i,1}$ and $x_{i,2}$ are estimated and then rearranged to solve for the adapted observer parameters φ_{obs} and A_{obs} at the current time t_k, such that:

$$\varphi_{obs,i,k} = \arctan(\frac{2\pi f_i \ \hat{x}_{i,1}}{\hat{x}_{i,2}}) - 2\pi f_i t_k \tag{7}$$

$$A_{obs,i,k} = \frac{\hat{x}_{i,1}}{\sin(2\pi f_i t_k + \varphi_{obs})}. \tag{8}$$

Finally, the prediction algorithm can be used to forecast the motion sequence over a prediction horizon T_{Pred}, i.e. at the time $t_k + T_{Pred}$. Referring to Equation

2, the predicted motion at $t_k + T_{Pred}$ is

$$s_{Pred}(t_k + T_{Pred}) = \sum_{i=1}^{N} A_{obs,i,k} \sin\left(2\pi f_i (t_k + T_{Pred}) + \varphi_{obs,i,k}\right) + v(t). \quad (9)$$

In the current work, the signals of interest are the ship's roll and pitch angles which the UAV can measure online using the ship motion detection algorithm from Abujoub et al. [41]. For the purposes of the current work, the SPA determines a *Go-NoGo* command based on the measured roll and pitch signals and the specified *Go* criteria. The criteria is compared with the predicted signal over the continuous prediction horizon T_{Pred}. Two SPAs are used in parallel to predict the ship's roll and pitch motion. If both magnitudes of the predicted signals are less than their threshold values a *Go* signal is enabled to initiate and/or continue a landing operation. To remove unwanted fluctuation in the *Go-NoGo* command signal, McPhee and Irani [40] use an algorithm that latches to a *Go* or *NoGo* command.

3.1.1. Go-NoGo Command Latching

The Go-NoGo command latching algorithm evaluates the incoming *Go-NoGo* commands from the SPA and latches to a command over an evaluation interval. Before re-evaluating and re-latching, a latched state will run for the selected time period, regardless of the incoming *Go-NoGo* states. For the current work, an evaluation interval of 0.25 s and latching period of 0.5 s were found to remove chatter and false *Go* signals in the SPA commands. In practice, physical tests should be used to evaluate both intervals which may change based on the system response times, rates-of-descent and operational modes.

3.1.2. SPA Prediction Horizon for Landing

During landing operations, the UAV transitions from its low hover state to a landing state if the predicted roll and pitch values are less than their thresholds. During landing, the prediction horizon T_{pred} input to the SPA decreases as a

function of the estimated remaining time to land. In the current study, the UAV will transition time from a 5 m or 2.5 m low hover to a grounded/landed state in 5 seconds. However, due to the heave motion of the ship, the time required to land may be less or exceed 5 seconds. Therefore, the prediction horizon of the SPA is constantly adjusted based off the estimated time to land.

Fig. 2 displays a flow diagram of the UAV landing procedure when using the SPA. When the UAV is above the landing zone, the SPA collects data to initialize. Once initialized, the UAV proceeds to its low hover position. The SPA's prediction horizon is adjusted based on the UAV's low hover position and landing velocity. If the roll and pitch predictions indicate it is safe to land, the SPA outputs a *Go* command, and the UAV lowers its altitude while also shortening the prediction horizon. While landing, if either the roll or pitch SPA predicts that the ship motion will exceed the threshold values, the system outputs *NoGo* and the UAV aborts the landing and returns to its low hover position. However, if the UAV is within 0.5 m of the deck it will land, based on the assumption that it is safer to land than to abort while in close proximity to the ship.

As an alternative to the SPA a new Landing Period Indicator method is proposed that can be used in lieu of or in addition to the SPA.

3.2. Landing Period Indicator (LPI)

The proposed Landing Period Indicator (LPI) is a system that, during an initialization/training period, determines a series of static and dynamic parameters which correlate the current ship motion to safe landing periods. The ability to determine the system parameters *in situ* is a considerable strength of the proposed method. Moreover, the ability to self-determine the system parameters regardless of the landing platform lends itself well to interoperability. For the LPI, the initialization period occurs at the same period in the landing operation as the SPA's initialization and is when the system parameters are determined. The proposed

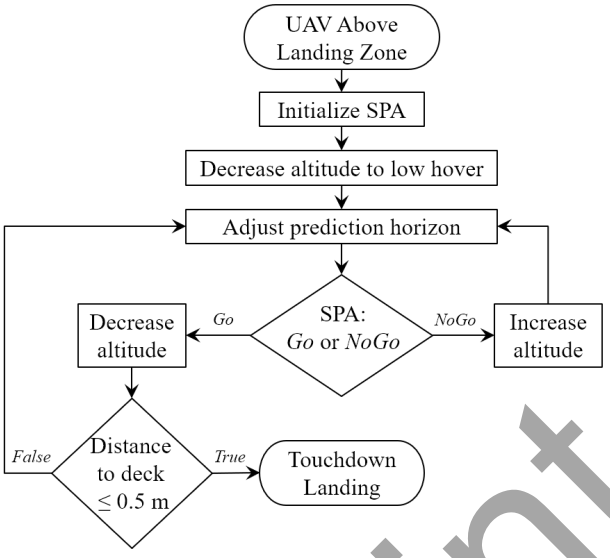

Figure 2: UAV landing protocol using the SPA.

LPI output $\Upsilon(t)$ is given by,

$$\Upsilon(t) = P_{\Upsilon}(t)\big(G_1\varepsilon(t) + G_2\bar{\varepsilon}(t)\big). \tag{10}$$

where $P_{\Upsilon}(t)$ is a time varying penalty function that is calculated online during the initialization period, G_1 and G_2 are static user determined weighting gains and $\varepsilon(t)$ and $\bar{\varepsilon}(t)$ are indicators of the total energy and time rate-of-change of the total energy in the signals of interest.

The top two plots of Fig. 3 show the $\pm 5^{\circ}$ roll and $\pm 2^{\circ}$ pitch ship motion thresholds from sea state 3 for a 120 second initialization period. The third plot of Fig. 3 shows the corresponding *Go-NoGo* results by using the UAV-LIDAR based ship motion detection algorithm [41]. The third plot also highlights in red when the *Go* value is sustained for 5 s or more and these *Go* periods are what the LPI will try to estimate. The last three plots of Fig. 3 plot the individual Energy Index (EI) for the signals of interest as a function of time which are used to determine the total energy values $\varepsilon(t)$ and $\bar{\varepsilon}(t)$ at time t.

The top plot of Fig. 4 plots the unpenalized LPI output, equation 10 without $P_\Upsilon(t)$, while the lower plot show the LPI final output Υ, equation 10, as a function of time for the same time period and conditions as Fig. 3. A value less than 1 for the final LPI indicates that the system is communicating a *Go* signal. The following subsections present how the various terms of the LPI output (Eqn. 10) are determined and constructed using the data of Figs. 3 and 4.

3.2.1. Energy ε:

The primary motions of interest to determine a safe landing time are the roll, pitch and heave. The other motions, yaw, sway and surge primarily govern flight stability and are used in tracking/homing methods. Hence for landing, ship roll velocity, pitch velocity and heave velocity were examined to estimate the kinetic energy of the system. Ideally, the kinetic energy K_e of the ship would be evaluated for each signal using $K_e = \frac{1}{2}mv_i^2$ where m is the mass/inertia of the ship, and v_i is the linear or angular velocity component of either roll, pitch or heave. In this work however, the mass of the ship is considered unknown but assumed to be constant; therefore, as a metric for ship energy, the Energy Index (EI) will be taken as the square of the velocity terms v_i^2. The units for heave energy is $\mathrm{m}^2/\mathrm{s}^2$ while the roll and pitch units are $\mathrm{deg}^2/\mathrm{s}^2$ or $\mathrm{rad}^2/\mathrm{s}^2$. To remove the units, each set of energy data is normalized using the average maximum value for each signal observed during the sustained *Go* periods of the initialization period. To remove data that could be anomalous or insignificant, the normalization coefficients are only computed in the initialization from the *Go* period values which are within half of a standard deviation of the cumulative average.

Denoted by $\varepsilon(t)$, the cumulative indicated EI of the ship is represented as the average value of the sum of the ship's normalized EIs and written as

$$\varepsilon(t) = \frac{1}{i}\sum_{i=1}^{6}\frac{v_i(t)^2}{N_i}, \tag{11}$$

where i represents the 6 axes of possible motion, $v_i(t)$ is the instantaneous velocity with respect to the i^{th}-axis at time t and N is the normalizing coefficient for the corresponding axis. A high ship energy implies high motion and is indicated when $\varepsilon(t) \geq 1$ where the ship may not be in a state at which the aircraft can safely land. For the primary motions of interest for aircraft landing, Eq. 11 can be written more specifically as

$$\varepsilon(t) = \frac{1}{3}\Big(\frac{\dot{p}(t)^2}{N_p} + \frac{\dot{q}(t)^2}{N_q} + \frac{\dot{w}(t)^2}{N_w}\Big), \tag{12}$$

where $\dot{p}(t)$, $\dot{q}(t)$, and $\dot{w}(t)$ are the ship's roll, pitch, and heave velocities at time t, while the corresponding static normalizing coefficients for roll, pitch and heave are N_p, N_q and N_w. These motions are used as they are part of the common Ship Helicopter Operating Limits [4, 5, 43]; however if required, additional axes could be included. Since the sea transfers energy to the ship, the rate-of-change of $\varepsilon(t)$ is an important factor in the LPI as the rate-of-change can indicate whether the system is volatile or in a lull. The normalized rate-of-change of the energy index $\bar{\varepsilon}(t)$ is taken as the absolute value of the derivative of the calculated EI

$$\bar{\varepsilon}(t) = N_\varepsilon \left| \frac{\partial \varepsilon(t)}{\partial t} \right|, \tag{13}$$

where N_ε is the unitless coefficient for $\bar{\varepsilon}(t)$, and is found using the same method used to calculate N_p, N_q, and N_w. The coefficient N_ε is used so that the order of magnitude of $\varepsilon(t)$ and $\bar{\varepsilon}(t)$ are comparable and their relative contributions to the LPI can be more easily adjusted by the user through weighting gains. The calculated energy index $\varepsilon(t)$ and its rate-of-change $\bar{\varepsilon}(t)$ are weighted and combined to form the basis of the landing period indicator $\Upsilon_B(t)$, such that

$$\Upsilon_B(t) = G_1\varepsilon(t) + G_2\bar{\varepsilon}(t), \tag{14}$$

where G_1 and G_2 are weighting static gains that alter the influence of the two energy parameters.

3.2.2. Weighting Gains G_1 and G_2

By weighting G_2 heavier than G_1, the LPI output value $\Upsilon(t)$ would be more sensitive to the rate-of-change of energy rather than the current energy. The weighting static gains may be adjusted to the desired performance, noting that they must always sum to 1. It was found that equal weighting had satisfactory results from the cases studied within the current work and future work could look at optimal determination of G_1 and G_2. The final term in the LPI, Eqn. 10, is the penalty function.

3.2.3. Penalty function P_Υ

Over the same 120 s period as Fig 3, the top plot of Fig. 4 displays the unpenalized LPI, Eqn. 14, where values under 1 are considered suitable for landing. The outlined area between 30 to 55 seconds of Fig. 4 suggests that there is an opportune landing period. However, referring to the third plot Fig. 3 one will notice that the same time period does not have a sustained *Go* period greater than 5 seconds as the pitch values are above and below the threshold values during the 30–55 s time period. A scenario that leads to the possible false LPI outputs is low frequency ship motion where the ship motion exceeds the threshold limits, such that Eqn. 12 and 13 output a low energy state. To combat these false positives during realtime execution, the LPI output $\Upsilon(t)$ will be constrained to only output a value less than 1, safe to land, if the current ship motion is within the threshold limits.

Furthermore, an initial ship motion penalty function $P'_\Upsilon(t)$ is introduced to the system to improve the LPI performance such that one can write an intermediate

output $\Upsilon'(t)$ in the form,

$$\begin{aligned}\Upsilon'(t) &= P'_{\Upsilon}(t)\Upsilon_B(t) \\ &= P'_{\Upsilon}(t)\big(G_1\varepsilon(t) + G_2\bar{\varepsilon}(t)\big).\end{aligned} \tag{15}$$

The penalty function amplifies the value of the LPI output when ship motion values are high. The penalty function takes the instantaneous measured roll and pitch values, $q(t)$ and $p(t)$, and scales them relative to their respective static thresholds: q_{max} and p_{max}. The average of the product from the pitch and roll RMS found during the initialization period is used as a constant gain for the penalty function. Thus, the initial penalty function $P'_{\Upsilon}(t)$ takes the general form

$$P'_{\Upsilon}(t) = \frac{p_{RMS}q_{RMS}}{2}\left(\left|\frac{q(t)}{q_{max}}\right| + \left|\frac{p(t)}{p_{max}}\right|\right). \tag{16}$$

If the roll and pitch RMS values, p'_{RMS} and q'_{RMS}, from the initialization are found to be less than 1, they are set as 1 such that the value of the penalty function is not lowered. Thus, p_{RMS} and q_{RMS} are expressed as,

$$p_{RMS} = \begin{cases} 1 & p'_{RMS} \leq 1 \\ p'_{RMS} & p'_{RMS} > 1 \end{cases}, \tag{17}$$

$$q_{RMS} = \begin{cases} 1 & q'_{RMS} \leq 1 \\ q'_{RMS} & q'_{RMS} > 1 \end{cases}. \tag{18}$$

Finally the penalty function $P_{\Upsilon}(t)$ is also restricted to be greater or equal to 1 such that

$$P_{\Upsilon}(t) = \begin{cases} 1 & P'_{\Upsilon}(t) \leq 1 \\ P'_{\Upsilon}(t) & P'_{\Upsilon}(t) > 1 \end{cases}. \tag{19}$$

$P_{\Upsilon}(t)$ is intended to never decrease the LPI value such that false Go signals are not introduced. Additionally, a delay function was implemented to prohibit the

system from indicating that it is safe to land immediately after a high LPI value is observed. The delay decreases the likelihood of a false LPI signal from occurring which may occur during ship velocity direction reversal, and was set to 1 s in the current work. For landing, the UAV compares the LPI output to the current ship motion and if both indicate that it is safe to land, the UAV proceeds to land and will only output *NoGo* if the LPI reading indicates *NoGo* and the current ship motion is outside the threshold limits.

The lower plot of Fig. 4 displays the final value of the LPI, $\Upsilon(t)$, with the penalty function where values of the LPI are the blue solid lines, and the opportune landing times are the red boxes. The LPI system outputs a *Go* signal if the LPI value is less than 1. The erroneous *Go* state previously identified between 30–55 s was removed in the final output of the LPI, lower plot. The final LPI outputs a value less than 1 for three of the five *Go* periods of the 120 s example data. Due to the penalty function, the LPI will output a conservative *NoGo* state in ship motion cases that are close to the threshold, such as those near found in the first 20 s of the example.

It is concluded that the LPI can reasonably estimate potential safe landing opportunities. With the LPI system developed, its effectiveness in determining *Go* states may be examined.

3.2.4. Comparison of LPI and SPA

To compare how well the LPI and the SPA can identify *Go* periods, the methods examined 15 test cases of simulated ship motion data. Ship motion sets were generated in ShipMo3D [44] and the sea states ranged from 2–6 while the heading of the 30 m ship heading was set to 30°, 60° and 90°. Each test case was 600 s in length, with the initial 120 s used to initialize the system while the remaining 440 s were used to compare the system's ability to correctly identify *Go* periods of 5 s and 3 s. The number of state changes between a *Go* and *NoGo*

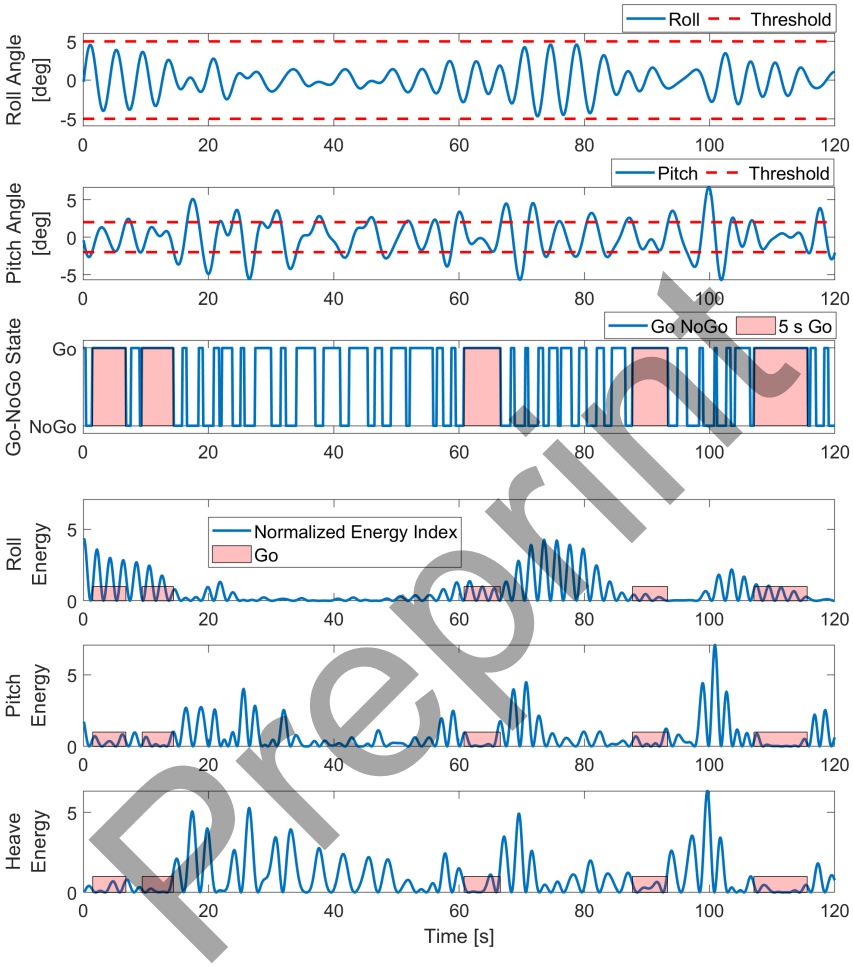

Figure 3: Data used during the initialization of the proposed LPI and development discussion of the LPI Plot 1) Roll vs Time with the 5° threshold; 2) Pitch vs Time with 2° threshold; 3) Calculated *Go-NoGo* based on plots 1 and 2, highlighted section indicate regions of *Go* periods greater than 5 s; 4) Roll Energy Index vs Time, with corresponding *Go* periods indicated from plot 3; 5) Pitch Energy Index vs Time, with corresponding *Go* periods indicated from plot 3; 6) Heave Energy Index vs Time, with corresponding *Go* periods indicated from plot 3

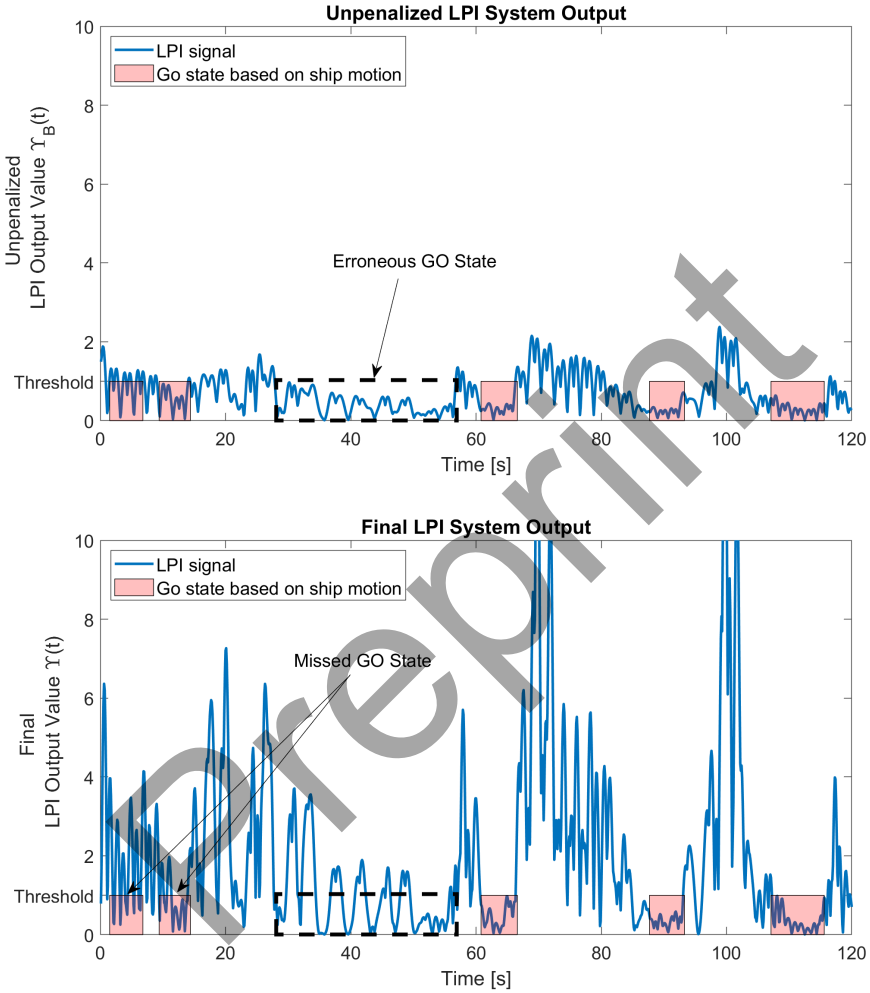

Figure 4: Top) The output of the unpenalized LPI system, *Go* periods are highlighted and correspond to the periods from Fig. 3. Dotted region indicates a potential erroneous *Go* period; Bottom) The output of the final LPI system where the system is able to successfully solve for three of the five *Go* periods.

command was also reported in order to investigate the effect of chatter between states. Table 1 outlines the efficiencies of the LPI and SPA, where efficiency is the percentage of time the systems correctly identified the sustained *Go* for 5 s and 3 s of sustained *Go* periods. The overall performance of each system is similar for 5 s, where the LPI and SPA had efficiencies of 56% and 59% respectively, while at 3 s the LPI and SPA had respective efficiencies of 70% and 72%. The average number of state changes from *Go* to *NoGo* was also similar, 25 to 21 for the LPI to the SPA respectively. It should be pointed out that for trial 13, the ship motion did not sustain a *Go* condition for longer than 5 s and neither system identified a *Go* period. From the comparison study it is expected that the results of using the LPI on the UAV will be similar to using the SPA. However, the LPI is considered to be less computationally expensive as there is no FFT nor large matrices to manipulate.

The LPI and the SPA system produce *Go-NoGo* commands but do not plan the trajectory of the UAV's autonomous descent. To accomplish the descent, an Active Heave Compensation (AHC) system is proposed which can be used in combination with the SPA and the LPI systems.

3.3. Active Heave Compensation (AHC)

There are two aspects of the proposed Active Heave Compensation (AHC) methodology for the UAV landing. First, while the UAV is station keeping at the low hover position, the risk of ship-UAV collision increases. Thus, a method to keep the UAV at a safe height, or to actively follow the ship's deck at a low hover, is required. Second, an AHC system can be used to project the landing trajectory of the dynamic ship motion and the anticipated landing time for the UAV.

3.3.1. AHC – Low Hover

Within the current study two low hover heights were examined: 2.5 m and 5 m. When the UAV was at the 5 m height, the risk of ship-UAV collision was

Table 1: Efficiencies and state changes for LPI system and SPA

Trial	Sea State	Heading [Deg]	LPI eff 5 s	SPA eff 5s	LPI eff 3 s	SPA eff 3 s	Go State Change LPI	Go State Change SPA
1	2	30	1.00	1.00	1.00	1.00	1	1
2		60	1.00	1.00	1.00	1.00	1	1
3		90	1.00	1.00	1.00	1.00	2	1
4	3	30	0.91	0.92	0.91	0.92	10	20
5		60	0.71	0.90	0.73	0.91	24	31
6		90	0.63	0.75	0.68	0.81	44	32
7	4	30	0.47	0.63	0.66	0.77	53	40
8		60	0.39	0.61	0.51	0.75	46	38
9		90	0.62	0.51	0.84	0.67	28	37
10	5	30	0.14	0.17	0.24	0.32	44	11
11		60	0.18	0.24	0.53	0.62	28	12
12		90	0.26	0.14	0.63	0.47	16	22
13	6	30	—	—	0.38	0.27	33	19
14		60	0.54	0.58	0.69	0.68	20	19
14		90	0.48	0.41	0.73	0.61	23	29
Average			0.56	0.59	0.70	0.72	25	21

never observed within the simulations; however, at the 2.5 m height, several ship-UAV collisions occurred during the initial testing. To combat these collisions, an AHC algorithm is proposed and utilizes an SPA similar to that used for roll and pitch predictions. However, instead of the SPA providing a *Go-NoGo* signal, the SPA returns an array of the predicted vertical distances between the ship and the UAV for the next 5 s with the computation of Eq. 9 at 100 Hz. To increase the precision of the prediction, a piece-wise spline is fit to the data at 1000 Hz. The up-sampling was necessary to provide a smooth trajectory for the landing while keeping the computation of the SPA low. Within the simulations, having the SPA algorithm output a more precise prediction of a smaller time step caused a

significant increase in the runtime. Additionally, it is noted that other smoothing and filtering techniques could be utilized to determine the trajectory; however, determining the *optimal* method of the landing trajectory is outside the scope of the current study but could be a worthwhile endeavour.

To reduce the risk of ship-UAV collision, the AHC system evaluates the predicted spline data for incoming high heave motion, where if a collision is anticipated, the AHC system will command the UAV to preemptively raise its altitude to avoid a collision. The system is not motion matching the ship which others have implemented [42, 28] but rather, the system is working to maintain a safe standoff distance while reducing the altitude variations of the UAV.

The prediction horizon t_{AHC}, over which the AHC system will search for incoming heave motion and compensate the UAV's position, should be tuned according with the aircraft's dynamic and flight characteristics. In the current work, the UAV had a maximum ascent rate of 0.5 m/s and descent -2.0 m/s, and using $t_{AHC} = 0.5$ s was effective in reducing UAV-ship collisions while at a 2.5 m low hover. Aside from actively searching for the future elevation of the ship deck and adjusting the UAV's low hover position, the AHC algorithm continually updates landing trajectories.

3.3.2. AHC – Landing Trajectories

The goal of trajectory planning is to search for a path which will result in a desired impact velocity between the UAV and ship. The trajectory planner operates as follows:

1. The AHC searches for UAV landing trajectories by taking the difference between the UAV's current position and the position of the ship deck for the next 5 s. As an example, Fig. 5 shows landing trajectories found by the AHC by showing the UAV's current position as a red dot and five example landing paths, the dotted magenta lines, that the UAV could travel

to the predicted position of the deck. The predicted heave motion is the red dotted-dashed line extending from the past heave motion, solid blue line. The black crosses at the end of the landing trajectories are the estimated points of touch down for the UAV. Each landing path requires a unique landing velocity to reach the ship deck at the specified time. In Fig. 5 only 5 landing trajectories are displayed, however, a landing trajectory is planned to reach every point in the predicted heave position array.

2. The predicted impact velocity between the UAV and the ship is found for each of the landing velocities by taking the difference between the landing velocities and the derivative of the ship's position at that moment in time. For the current study, the target impact velocity is 0.5 m/s and the greatest allowable impact velocity is 1 m/s; however, these target values can be user adjusted.

3. A gradient search is performed on the predicted impact velocities to search for a landing velocity which most closely meets the goal of 0.5 m/s. If the impact velocity is unobtainable, a search is performed for a impact velocity of 0.5 ± 0.1 m/s until a match is found. If multiple landing trajectories meet the goal value, the trajectory which occurs the soonest is selected.

4. If a *Go* command is received for landing, the UAV will follow the planned landing trajectory. During descent the UAV continues to search for landing trajectories that are closest to the impact velocity goal, and if one is found the UAV will alter its descent.

5. At anytime during landing, if a *NoGo* signal is received the UAV will return to its low hover position unless the relative distance between the vessel and the craft is less than 0.5 m.

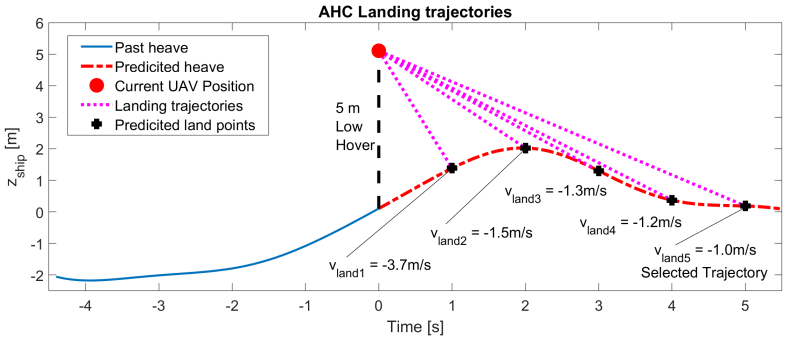

Figure 5: Schematic of possible landing trajectories for the UAV.

3.3.3. Landing Trajectories and Prediction Horizon

In the current work there are three landing descent modes. These modes are used to reflect a pilot's discretion of the rate of descend [5] for various conditions. The landing mode attempts to land the UAV within 5 s. Additionally, the landing mode affects how the prediction horizon is calculated when the AHC is used with an SPA to forecast *Go-NoGo* states.

Landing Mode 1 (M_1) corresponds to a low hover position of 2.5 m above the ship deck and a landing velocity in m/s of,

$$V_{L;M_1} = -0.5, \tag{20}$$

giving the prediction horizon,

$$T_{Pred;M_1}(t) = \frac{L_d(t)}{V_{L;M1}}, \tag{21}$$

where $L_d(t)$ is the instantaneous distance to the ship deck measured by the UAV's systems. The dynamic prediction horizon $T_{Pred(M_1)}(t)$ is used when the UAV is using the SPA for *Go-NoGo* states but without AHC.

Landing Mode 2 (M_2) has a low hover of 5 m and follows a piece-wise function

to determine its linear-ramp landing velocity,

$$V_{L;M_2}(t) = \begin{cases} -2 \ \frac{m}{s} & L_d(t) > 3 \ m \\ -1 \ \frac{m}{s} & 3 \ m \leq L_d(t) > 1 \ m \\ -0.5 \ \frac{m}{s} & 1 \ m \leq L_d(t) \end{cases} . \tag{22}$$

The landing velocities from Eq. 22 are used to calculate prediction horizon of an SPA for *Go-NoGo* states such that,

$$T_{Pred;M_2}(t) = \begin{cases} \frac{L_d(t)-3}{|V_{L;M2}|} + 4 & L_d(t) > 3 \ m \\ \frac{L_d(t)-1}{|V_{L;M2}|} + 2 & 3 \ m \leq L_d(t) > 1 \ m \\ \frac{L_d(t)}{|V_{L;M2}|} & 1 \ m \leq L_d(t) \end{cases} , \tag{23}$$

where the constants 4 and 2 are the remaining time it will take the UAV to cycle through the next piece-wise function(s) until the UAV has landed without the use of AHC.

Using AHC, Landing Mode 3 (M_3) is applied to both 2.5 or 5 m low hover positions. Mode 3 has a dynamic landing velocity that is a function of the distance from the ship deck and the remaining time to landing. The dynamic landing velocity is calculated as

$$V_{L;M_3}(t) = \frac{z_{ship}(t) - L_d(t)}{T_{land}(t)}, \tag{24}$$

where $L_d(t)$ is the UAV's instantaneous measurement of the UAV's height above the ship deck, $z_{ship}(t)$ is the estimated ship deck height at landing which is found through the AHC landing algorithm (section 3.3.1) and $T_{land}(t)$ is the remaining time to the estimated landing, also found via the AHC algorithm. To prevent excessive downward velocity the UAV is limited to -2 m/s. Once initiated, the system attempts to land the UAV in T seconds or less regardless of the relative

positions; thus, in Mode 3, during landing the SPA prediction horizon is

$$T_{Pred;M_3}(t) = \begin{cases} T - \Delta t_{land} & T > \Delta t_{land} \\ 0 & T \leq \Delta t_{land} \end{cases} . \quad (25)$$

where $\Delta\ t_{land}$ is the elapsed time since the *Go* signal was received and T is taken as 5 s in the current work.

3.3.4. Performance of AHC for landing

To evaluate the performance of the AHC without the addition of the SPA estimating the safe opportunities to land, four test cases were examined:

Case 1: Low hover 2.5 m without AHC (Mode 1)

Case 2: Low hover 2.5 m with AHC (Mode 3)

Case 3: Low hover 5.0 m without AHC (Mode 2)

Case 4: Low hover 5.0 m with AHC (Mode 3)

Each of the cases were tested under a variety of sea conditions and neither an SPA nor an LPI were used to estimate opportune safe landing times. Landing was initiated 200 s into the simulation. The various tests comprised of ship motion in sea states 4, 5 and 6 with ship headings of 30°, 60°, and 90°. To ensure a controlled testing environment, atmospheric turbulence and wind gusts were disabled in the model. For the descent velocity, case 1 and 3 used Eq. 20 and 22 respectively, while case 2 and 4 both used Eq. 25 and 24.

Table 2 summarizes the landing velocity results obtained from the tests. The AHC 2.5 m and 5 m low hover cases both had 3 tests land with an impact velocity greater than 1 m/s. In contrast, the cases without the AHC had 6 and 7 tests with an impact velocity greater than 1 m/s. Using the AHC, the average landing velocities for both low hover cases were below 1 m/s, however, the average did not

Table 2: Impact velocity comparison between using the standard landing methods and using the active heave compensation algorithm for headings of 0°, 30°, 60°, and 90° in sea states 4, 5, and 6

Landing Mode	Low Hover Position [m]	# of Trials with Landing Velocity >1 m/s (out of 9)	Avg. Landing Velocity [m/s]	Std. Landing Velocity [m/s]
No AHC	2.5	6	0.94	0.51
AHC	2.5	3	0.68	0.38
No AHC	5	7	1.16	0.52
AHC	5	3	0.80	0.41

meet the goal impact velocity of 0.5 m/s. Furthermore, the standard deviation values of the landing velocity are lower with the AHC system indicating that the system is more consistent. The results indicate that using signal prediction for determining landing trajectories can improve landing performance. Now that the proposed methodologies are fully defined the next section examines a series of comparative case studies.

4. Case Studies

A simulation was constructed within Matlab and Simulink which uses ship motion data from ShipMo3D [44]. The UAV model incorporates validated, motor dynamics [45], propeller theory [46], ground effects [47], aerodynamic effects [48], steady wind and gusts [49, 50], and atmospheric turbulence [50]. Traditional proportional-integral-derivative based control methodologies were used for the altitude, yaw, roll, pitch and tracking. The methodology for determining the relative motion of the UAV and the ship using a simulated LIDAR can be found in the work of Abujoub et al. [41]. For the ship motion, ShipMo3D was used to simulate a 30 m vessel travelling at speeds of 6, 8 and 10 kn, through sea states

2 to 6 and with headings from 0° to 180° in increments of 30°. The landing zone is 11 m behind and 1.5 m above the ship's centre-of-gravity.

There is a strong correlation between the sea state and the wind [51]; thus, the wind velocities were 3.75, 6.4, 9.4 m/s for sea states 2, 3 and 4. Sea-state 5 and 6, however, used a saturated wind velocity of 10 m/s as the modelled UAV could not maintain controlled flight in sustained winds above 10 m/s. The critical aspect of the presented work focuses on the landing methodologies and not the UAV's ability to reject wind disturbances. The primary input into the landing methodologies is the ship motion while the wind is a disturbance to the system. Future users should confirm their performance characteristics of the vehicles prior to deployment.

As a benchmark, an "unregulated" system was used to compare the SPA, LPI and AHC landing methodologies with each possible permutation examined:

Method 1: Unregulated (Benchmark)

Method 2: SPA

Method 3: LPI

Method 4: AHC

Method 5: SPA + LPI

Method 6: SPA + AHC

Method 7: LPI + AHC

Method 8: SPA + LPI + AHC

With the benchmark system, Method 1, the UAV will descend if the *current* ship's instantaneous motion is within the motion limits or ascend to the low hover if the motion is outside the limits. Method 2 uses the SPA to predict when

the roll and pitch values will be below their respective thresholds for at least 5 seconds and attempt to land the UAV when it predicts a safe moment. Method 3 utilises the LPI, Eq. 15, to determine the *Go* and *NoGo* landing commands. In Method 4 the AHC system assists the UAV to maintain a minimum low hover position above the ship and plans the landing trajectories. Method 5 combines the LPI and SPA, where the UAV will land if a *Go* state is found by both the SPA and the LPI. In Method 6 the SPA determines the *Go* states and the AHC assists the UAV to maintain the low hover position while also planning the landing trajectories. Method 7 combines LPI to determine *Go* states and the AHC for landing trajectories. Finally, Method 8 uses the SPA and LPI, where both systems need to latch on a *Go* state before the UAV will use the AHC landing trajectories.

A landing is deemed successful if the UAV contacted the ship when the ship's pitch was less than $\pm 2^\circ$, roll less than $\pm 5^\circ$ and with a relative impact velocity less than or equal to 1 m/s. Additionally, each method was performed with two different low hover altitudes: 2.5 m and 5 m. When landing from 2.5 m, the UAV used a 0.5 m/s descent velocity (Mode 1) and when landing from 5 m, the UAV followed a piece-wise landing velocity (Mode 2). However, if using the AHC (Mode 3), the system will determine the landing trajectory for the UAV as outlined in Section 3.3. The top plot of Fig. 6 provides a summary of the results for the 8 methods in the 2.5 metre low hover stand-off while the bottom half of Fig. 6 details the 5 metre low hover stand-off. Of the 105 cases per method, the figure provides the number of times when the UAV successful landed, landed outside the roll $\pm 5^\circ$ and pitch $\pm 2^\circ$ limits, landed when the impact velocity exceeded the 1 m/s, failed to land within 10 min, landed in a *NoGo* state, and the average number of state changes for each method. Table 3 provides the same data for the various methods but as a function of the sea state while Table 4 provides a tabulated summary of the results for each methodology.

For each sea state examined, the ship's velocity was varied between 6, 8 and

10 kt and the heading was varied from 0° to 180° in increments of 30°, which results in 105 test per landing methodology, or 21 test per row of Table 3. The following two sections discuss the findings from Fig. 6 and Tables 3 and 4 from the two different low over heights.

4.1. Results – Low Hover, 2.5 m

Examining the top half of Fig 6, it is observed that the individual SPA, LPI and AHC all improve the landing performance over the benchmark unregulated system. However, limitations are observed for each methodology; compared to the benchmark, the SPA had the greatest increase in the number of successful landings but also had the highest number of landings in a *NoGo*. Comparing the LPI to the benchmark, there is an increase in the number of successful landings by 13% but the LPI has a significant number of landings which exceeded the velocity limits. The AHC system was only able to land 2 additional times when compared to the unregulated system, but there was an increase in the number of times that a landing occurred when the system was not within the pitch and roll limits. The results suggest that the sole implementation of the SPA, LPI or AHC could improve the number of landings but one risks landing in unfavorable scenarios that could possibly damage the ship or aircraft.

The combination systems, SPA+LPI, SPA+AHC and LPI+AHC improved landing over the individual methodologies and the benchmark. All of the combined methods successfully landed 87 times, an increase of 24% over the benchmark. Examining the SPA+AHC, there are an additional 9 landings when the system touched down in a *NoGo*, compared to the 4 occurrences of unregulated benchmark method. However, when comparing the SPA+AHC to the SPA method, there is a decrease from 11 to 9 times when the system landed in a *NoGo*. The same trend is also shared by the SPA+LPI system when compared to SPA method. When one compares the LPI and SPA+LPI method there is an

increase from 4 to 9, in the number of times when the system landed in a *NoGo*. However, for the SPA+LPI and LPI method comparison, the other metrics have all improved when the LPI is combined with the SPA. In general, using the combined SPA or LPI with the AHC to help plan the trajectories improved all of the metrics, with the exception of the unit increase for the average number of state changes for the SPA+AHC method. Since the SPA+AHC had the least number of landings outside of the roll and pitch limits, it could be considered superior the SPA+LPI, followed by the SPA+LPI and then the LPI+AHC method.

The combined LPI+SPA+AHC method, resulted in the highest number of successful landings, 93 of a possible 105, a 33% increase and the greatest improvement in all of the metrics. The combined LPI+SPA+AHC system is favoured and suggested for advancement over all other methodologies. Table 4 indicates the mechanisms of the 12 failed landings of the LPI+SPA+AHC. Of the failed landings, 8 were due to the UAV landing in periods of high ship motion and 6 were from high impact velocities, meaning that there was an overlap of 2 trials which failed to land within the motion thresholds and velocity limit. For the LPI+SPA+AHC, 7 of the failed landings occurred during a *NoGo* condition indicating that the UAV was intercepted by the ship.

Examining Table 3 and 4, the 2.5 m trials all had a 100% successes rate for landing in sea states 2 and 3, except when using the LPI, which had a case where the ship motion threshold and impact velocity limit were exceeded. Using the LPI+SPA method was the only landing system with a 100 % success rate in sea-state 4, followed by the LPI and LPI+SPA+AHC systems, which each had 19 out of 21 successful landings. There was a sharp decline in landing performance for all test cases in sea state 5, with the landing with LPI+SPA and LPI+SPA+AHC methods having the best performances, 14 successful landings each. The other regulated systems were up to 2 successful landings behind, where as the unregulated benchmark system only had 8 successful landings in sea state 5.

Based off the results in Fig. 6 and Tables 3 and 4 the ranking from best performing to worst performing landing methodologies from a 2.5 m low hover are:

1. LPI+SPA+AHC
2. SPA+AHC
3. LPI+SPA
4. LPI+AHC
5. SPA
6. LPI
7. AHC
8. Unregulated (Benchmark)

4.2. Results – Low Hover, 5 m

The lower half of Fig. 6 highlights the results for the 5 m landing tests. Similar to the 2.5 m results, using LPI+SPA+AHC outperformed all other landing methods. The LPI+SPA+AHC successfully landed 94 out of the 105 trials with 1 failed landing due to ship motion and 1 due to impact velocity. The LPI+SPA+AHC has 9 cases where the UAV did not land within the 600 s simulation — 7 in sea state 5 and 2 in sea state 6. The LPI+AHC method also had 94 successful simulations; however, the method results in an increased number of landings outside the safe roll and pitch limits — 11 in total.

Overall, every method outperformed the unregulated benchmark method. It is observed that the methods utilizing the SPA have a significant increase in the number of landings within the ship motion thresholds. The addition of the AHC improved the landing success while reducing the impact velocities. The LPI was

found to improve the landing performance compared to the unregulated system, however, when not combined with either the SPA or AHC system, the results were poor in comparison to the other systems using SPA and AHC. Similar to the 2.5 m cases, the state changes from *Go* to *NoGo* are all comparable, with the LPI having the least number of state changes. For the 5 m cases, the unregulated system had the fewest successful landings, but also had a high number of landings during *NoGo* conditions and high impact velocities. The UAV using the SPA had 2 cases during sea state 6 where the UAV crashed due to rapid landing state changes combined with the ship movement and environmental disturbances that overwhelmed the UAV's control efforts.

For the 5 m low hover test, Tables 3 and 4 show all landing methods had a 100% success rate for landing in sea state 2, and methods in combination with AHC had 100% success in sea state 3. In sea state 3 and above, the unregulated method decreased in landing performance, where as the other systems had a more gradual decrease. The LPI+AHC and LPI+AHC+SPA methods had a 100% landing success rate in sea state 4. The highest performing system in sea state 5 was LPI+AHC, which had 15 successful landings. The 5 m results in Table 3 indicate that using the SPA leads to safer UAV operation, however, the potential inability to land in higher sea states is an avenue for future work. The LPI+AHC was found to be the most successful landing system in sea state 5, having safely landed 15 of 21 cases. The top performing method in sea state 6 is the LPI+AHC+SPA, where 18 of 21 cases landed successfully. Overall, the LPI+AHC+SPA system showed an improvement of 34% when compared to the benchmark. Similar to the 2.5 m LH cases, there was a correlation between an increase in the number of state changes and failed landings to the increase in sea state.

The overall ranking from best performing to worst performing landing systems for the 5 m test cases are:

1. LPI+SPA+AHC
2. LPI+AHC
3. SPA+AHC
4. LPI+SPA
5. SPA
6. LPI
7. AHC
8. Unregulated (Benchmark)

4.3. Discussion

From the case study results, using any of the landing methods proposed in this work improves UAV landing performance when compared to the benchmark unregulated system. Both the LPI and SPA are effective in determining *Go* states, however, the effectiveness is increased when paired with each other. The AHC reduces the impact velocity between the UAV and ship and as a single system it had the least number of landings which exceeded the impact velocity. When added to LPI and SPA, the AHC system further reduced the number of landings that exceeded the impact velocity.

The overall best landing performance for both low hover cases was LPI + SPA + AHC method. The combined method had an increase of over 32% in successful landings when compared to the benchmark. However, each method has its strengths and weaknesses. For instance, the unregulated system is best suited for landing during sea states 3 and below. At these low sea states the unregulated landing success rate is the same as the regulated systems, but on average the UAV was able to land within the first 66 s of the simulation whereas the other

Table 3: Expanded results of 2.5 and 5 m low hover simulations

Method	Sea State	Successful Landing of 21 Trials		Failed to Land within Roll or Pitch Limit		Exceeded Impact Velocity Limit		UAV did not Land		Landed in *NoGo* State		Avg. Landing State Change (*NoGo*-*Go*)	
		2.5m	5m	2.5m	5m	2.5m	5m	2.5m	5m	2.5m	5m	2.5m	5m
Unregulated	2	21	21	0	0	0	0	0	0	0	0	1	1
	3	21	19	0	0	0	2	0	0	0	0	3	1
	4	11	15	4	4	6	5	0	0	0	3	4	3
	5	8	7	6	9	10	12	0	0	1	6	4	9
	6	9	8	6	7	12	12	0	0	3	3	4	6
SPA	2	21	21	0	0	0	0	0	0	0	0	1	1
	3	21	21	0	0	0	0	0	0	0	0	1	1
	4	18	17	0	0	3	4	0	0	0	0	4	3
	5	13	12	4	2	6	4	0	3	4	0	4	5
	6	9	14	7	2	9	5	0	2*	7	0	2	6
LPI	2	21	21	0	0	0	0	0	0	0	0	1	1
	3	20	18	1	3	1	3	0	0	0	1	1	1
	4	19	14	1	5	2	7	0	0	0	0	2	2
	5	11	14	8	6	9	7	0	0	1	0	2	3
	6	8	11	9	5	12	10	0	0	3	0	2	3
AHC	2	21	21	0	0	0	0	0	0	0	0	1	1
	3	17	18	2	2	2	2	0	0	1	1	2	2
	4	12	10	7	7	2	5	0	0	0	2	5	5
	5	11	16	8	3	7	2	0	0	1	0	12	16
	6	11	11	6	6	4	3	0	0	1	0	10	14
SPA+LPI	2	21	21	0	0	0	0	0	0	0	0	1	1
	3	21	20	0	0	0	0	0	0	0	0	1	1
	4	21	20	0	1	0	0	0	0	0	0	4	3
	5	14	13	5	1	5	2	0	5	5	0	3	4
	6	10	11	7	3	10	8	0	0	7	1	2	4
SPA+AHC	2	21	21	0	0	0	0	0	0	0	0	1	1
	3	21	21	0	0	0	0	0	0	0	0	2	2
	4	17	16	1	3	3	2	0	0	1	0	3	3
	5	13	14	4	0	4	1	0	6	5	0	4	7
	6	15	15	3	0	5	4	0	2	3	0	3	8
LPI+AHC	2	21	21	0	0	0	0	0	0	0	0	1	1
	3	21	21	0	0	0	0	0	0	0	0	1	1
	4	18	21	3	0	0	0	0	0	0	0	2	3
	5	12	15	8	6	3	4	0	0	1	1	2	5
	6	15	16	5	5	3	2	0	0	3	0	3	4
LPI+SPA+AHC	2	21	21	0	0	0	0	0	0	0	0	1	1
	3	21	21	0	0	0	0	0	0	0	0	1	1
	4	19	21	2	0	0	0	0	0	0	0	2	3
	5	14	13	4	1	3	0	0	7	4	0	2	5
	6	18	18	2	0	3	1	0	2	3	0	2	5

* 2 out of the 5 UAVs crashed

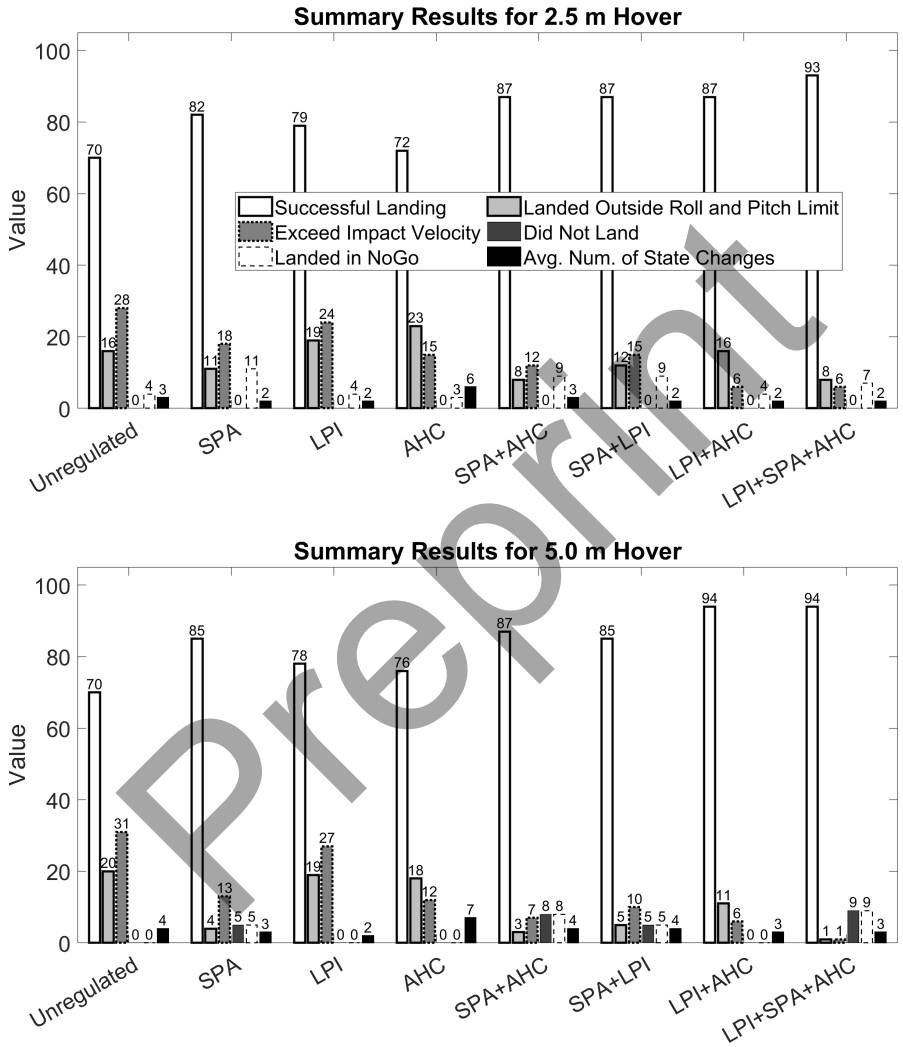

Figure 6: Summary Results of Landing Methodologies for the 2.5 and 5 metre hover simulation. Sea states range from 2–6; A total of 105 trials were performed for each system

Table 4: Summary results of 2.5 and 5 m low hover simulations

Method	Successful Landing of 105 Trials		Failed to Land within Roll or Pitch Limit		Exceeded Impact Velocity Limit		UAV did not Land		Landed in *NoGo* State		Avg. Landing State Change (*NoGo-Go*)	
	2.5m	5m	2.5m	5m	2.5m	5m	2.5m	5m	2.5m	5m	2.5m	5m
Unregulated	70	70	16	20	28	31	0	0	4	12	3	4
SPA	82	85	11	4	18	13	0	5*	11	0	2	3
LPI	79	78	19	19	24	27	0	0	4	1	2	2
AHC	72	76	23	18	15	12	0	0	3	3	6	7
SPA+AHC	87	87	8	3	12	7	0	8	9	0	3	4
SPA+LPI	87	85	12	5	15	10	0	5	9	1	2	4
LPI+AHC	87	94	16	11	6	6	0	0	4	1	2	3
LPI+SPA+AHC	93	94	8	1	6	1	0	9	7	0	2	3

* 2 out of the 5 UAVs crashed

methods had a cumulative average of 215 s. In higher sea states, using the LPI or the SPA could be advantageous. The SPA showed overall better performance than the LPI, however, there were cases for the 5 m low hover where, when using the SPA, the UAV was unable to land. The UAV being unable to land may be viewed as positive or negative. Depending on the scenario, it could be argued that not landing at all is better than landing unsafely. Nevertheless, there may be times when it might be more dangerous to loiter above the ship deck in adverse conditions than it would be to attempt a landing. An advantage of the LPI is its simple implementation and computational efficiency and effectiveness for a non-predictive system. The LPI would be suitable as a stand alone landing system up to sea state 4, where after the decreased forecast performance may endanger the UAV or deck crew. From the results, it is not recommended to use the SPA as a stand-alone system above sea states 4, however, if forced to land during higher sea states, using the SPA will increase the potential of a safe landing. The addition of AHC can be used in any sea state, however, it is most recommended to be used in any sea state greater than 3. As stated, combining the LPI, SPA, and AHC significantly increases the likelihood of a successful landing, and it is

recommended to be used in any sea state greater than 3.

5. Conclusions

This paper presented the construction of a signal prediction algorithm along with the development of a new landing period indicator and active heave compensation system for UAVs attempting to land on moving maritime vessels. The signal prediction algorithm is able to make short-term forecasts of periodic motion to estimate and predict the ship motion so that a UAV could make autonomous landings. Additionally, the signal prediction algorithm was used to construct an active heave compensation system for the UAV which was used to determine landing trajectories of the UAV. The landing period indicator uses an estimate of the ship's energy to determine if there is a quiescent period of ship motion. The gains and parameters of the SPA system must be tuned *a priori* which is a limitation of the system; however, all tuning parameters were held constant in the 105 test cases which spanned from sea state 2–6, headings from 0° to 180° and ship velocities of 6, 8 and 10 knots. The new landing period estimator tunes itself *in situ* during an initialization period while in the hover state just prior to the final descent. These systems can be used individually or in combination with one another. Overall, the system which performed the best used all three of methods and the UAV was able to successfully land within the defined operating conditions in over 88% of the test cases. It was found that the low hover height did influence the mode at which each system failed. Thus, further work and risk assessment is suggested to determine the optimal low hover height for small UAVs. Future work will involve laboratory testing of these methodologies along with optimization studies of parameters within individual methods. A key feature of the proposed methodologies is that they promote interoperability as there is no specialized ship equipment that is required to facilitate the landing or

final descent.

Acknowledgements

The authors acknowledge the support of the Natural Sciences and Engineering Research Council of Canada (NSERC), [funding reference number 06967]. Cette recherche a été financée par le Conseil de recherches en sciences naturelles et en génie du Canada (CRSNG), [numéro de référence 06967]. Additionally, we would like to acknowledge Kraken Robotic Systems Inc. for their feedback in the work, and Carleton University for their support. The authors would like to thank DSA LTD (Dynamic Systems Analysis Ltd) for the in-kind donation of ShipMo3D.

References

[1] M. Faria, J. Pinto, F. Py, J. Fortuna, H. Dias, R. Martins, F. Leira, T. A. Johansen, J. Sousa, K. Rajan, Coordinating UAVs and AUVs for oceanographic field experiments: Challenges and lessons learned, in: 2014 IEEE International Conference on Robotics and Automation (ICRA), IEEE, 2014, pp. 6606–6611.

[2] S. Yeong, L. King, S. Dol, A review on marine search and rescue operations using unmanned aerial vehicles, Int. J. Mech. Aerosp. Ind. Mech. Manuf. Eng 9 (2) (2015) 396–399.

[3] J. Fortuna, F. Ferreira, R. Gomes, S. Ferreira, J. Sousa, Using low cost open source uavs for marine wild life monitoring-field report, IFAC Proceedings Volumes 46 (30) (2013) 291–295.

[4] United States Coast Guard, Shipboard-helicopter operational procedures manual, Tech. Rep. COMDTINST 3710.2D (October 2001).

[5] North Atlantic Treaty Organization (NATO), Helicopter operations from ships other than aircraft carriers (hostac), Tech. Rep. MPP-02, NATO (April 2017).

[6] F. Santoso, M. A. Garratt, S. G. Anavatti, State-of-the-art intelligent flight control systems in unmanned aerial vehicles, IEEE Transactions on Automation Science and Engineering 15 (2) (2017) 613–627.

[7] J. Alvarenga, N. I. Vitzilaios, K. P. Valavanis, M. J. Rutherford, Survey of unmanned helicopter model-based navigation and control techniques, Journal of Intelligent & Robotic Systems 80 (1) (2015) 87–138.

[8] L. A. S. Velásquez, Modeling and control techniques of autonomous helicopters for landing on moving platforms, Ph.D. thesis, Universidad de Sevilla (2016).

[9] North Atlantic Treaty Organization (NATO), Interoperability standards and profiles, NATO Interoperability Standards and Profiles ADatP-34(K)-REV1, C3B Interoperability Profiles Capability Team (August 2018).

[10] C. Patruno, M. Nitti, A. Petitti, E. Stella, T. D'Orazio, A vision-based approach for unmanned aerial vehicle landing, Journal of Intelligent & Robotic Systems 95 (2) (2019) 645–664.

[11] J. L. Sanchez-Lopez, J. Pestana, S. Saripalli, P. Campoy, An approach toward visual autonomous ship board landing of a VTOL UAV, Journal of Intelligent & Robotic Systems 74 (1-2) (2014) 113–127.

[12] L. Wang, X. Bai, Quadrotor autonomous approaching and landing on a vessel deck, Journal of Intelligent & Robotic Systems 92 (1) (2018) 125–143.

[13] J. L. Sanchez-Lopez, S. Saripalli, P. Campoy, J. Pestana, C. Fu, Toward visual autonomous ship board landing of a vtol UAV, in: 2013 International conference on unmanned aircraft systems (ICUAS), IEEE, 2013, pp. 779–788.

[14] S. Arora, S. Jain, S. Scherer, S. Nuske, L. Chamberlain, S. Singh, Infrastructure-free shipdeck tracking for autonomous landing, in: 2013 IEEE international conference on robotics and automation, IEEE, 2013, pp. 323–330.

[15] W. Kong, D. Zhang, X. Wang, Z. Xian, J. Zhang, Autonomous landing of an UAV with a ground-based actuated infrared stereo vision system, in: 2013 IEEE/RSJ International Conference on Intelligent Robots and Systems, IEEE, 2013, pp. 2963–2970.

[16] P. Moriarty, R. Sheehy, P. Doody, Neural networks to aid the autonomous landing of a UAV on a ship, in: 2017 28th Irish Signals and Systems Conference (ISSC), IEEE, 2017, pp. 1–4.

[17] A. Benini, M. J. Rutherford, K. P. Valavanis, Real-time, gpu-based pose estimation of a UAV for autonomous takeoff and landing, in: 2016 IEEE International Conference on Robotics and Automation (ICRA), IEEE, 2016, pp. 3463–3470.

[18] Y. Meng, W. Wang, H. Han, J. Ban, A visual/inertial integrated landing guidance method for UAV landing on the ship, Aerospace Science and Technology 85 (2019) 474–480.

[19] L. A. Sandino, M. Bejar, K. Kondak, A. Ollero, On the use of tethered configurations for augmenting hovering stability in small-size autonomous helicopters, Journal of Intelligent & Robotic Systems 70 (1-4) (2013) 509–525.

[20] S.-R. Oh, K. Pathak, S. K. Agrawal, H. R. Pota, M. Garrett, Autonomous helicopter

landing on a moving platform using a tether, in: Proceedings of the 2005 IEEE International Conference on Robotics and Automation, IEEE, 2005, pp. 3960–3965.

[21] S.-R. Oh, K. Pathak, S. K. Agrawal, H. R. Pota, M. Garratt, Approaches for a tether-guided landing of an autonomous helicopter, IEEE Transactions on Robotics 22 (3) (2006) 536–544.

[22] R. Langlois, P. Keary, Methodology for ensuring safety of an embarked helicopter securing system probe installation, in: Proceedings of International Congress of the Aeronautical Sciences, Toronto, Canada, 2002.

[23] J. Ross, M. L. Seto, C. Johnston, Zero visibility autonomous landing of quadrotors on underway ships in a sea state, in: 2019 IEEE International Symposium on Robotic and Sensors Environments (ROSE), IEEE, 2019, pp. 1–7.

[24] H. Razmi, S. Afshinfar, Neural network-based adaptive sliding mode control design for position and attitude control of a quadrotor UAV, Aerospace Science and Technology 91 (2019) 12–27.

[25] M. Garratt, S. Anavatti, Non-linear control of heave for an unmanned helicopter using a neural network, Journal of Intelligent & Robotic Systems 66 (4) (2012) 495–504.

[26] J. R. Hervas, M. Reyhanoglu, H. Tang, Automatic landing control of unmanned aerial vehicles on moving platforms, in: 2014 IEEE 23rd international symposium on industrial electronics (ISIE), IEEE, 2014, pp. 69–74.

[27] T. D. Ngo, C. Sultan, Nonlinear helicopter and ship models for predictive control of ship landing operations, in: AIAA Guidance, Navigation, and Control Conference, 2014, p. 1298.

[28] K. Xia, S. Lee, H. Son, Adaptive control for multi-rotor uavs autonomous ship landing with mission planning, Aerospace Science and Technology 96 (2020) 105549.

[29] Y. Huang, M. Zhu, Z. Zheng, M. Feroskhan, Fixed-time autonomous shipboard landing control of a helicopter with external disturbances, Aerospace Science and Technology 84 (2019) 18–30.

[30] B. Ferrier, R. Ernst, Fire scout launch and recovery considerations in unexpected ship roll motion conditions, Naval Engineers Journal 129 (4) (2017) 87–98.

[31] C. Fourie, The autonomous landing of an unmanned helicopter on a moving platform, Ph.D. thesis (2015).

[32] B. Ferrier, T. Manning, Simulation and testing of the landing period designator (lpd) helicopter recovery aid, Naval engineers journal 110 (1) (1998) 189–205.

[33] B.-G. Huang, Z.-J. Zou, Short-term prediction of ship pitching motion based on artificial

neural networks (2016).

[34] X.-Y. Peng, X.-R. Zhao, Q.-F. Gao, Research on real-time prediction algorithm of ship attitude motion, Journal of System Simulation 19 (2) (2007) 267–271.

[35] Y. Chen, J. Ye, X. Zhang, Experiment of extremely short-term prediction of ship motion, Ship & Ocean Engineering 39 (1) (2010) 13–15.

[36] X. Zhao, R. Xu, C. Kwan, Ship-motion prediction: algorithms and simulation results, in: 2004 IEEE International Conference on Acoustics, Speech, and Signal Processing, Vol. 5, IEEE, 2004, pp. V–125.

[37] J. C. Chung, Z. Bien, Y. S. Kim, A note on ship-motion prediction based on wave-excitation input estimation, IEEE Journal of oceanic engineering 15 (3) (1990) 244–250.

[38] Z. Zhen, S. Jiang, K. Ma, Automatic carrier landing control for unmanned aerial vehicles based on preview control and particle filtering, Aerospace Science and Technology 81 (2018) 99–107.

[39] J. K. Woodacre, R. J. Bauer, R. A. Irani, Hydraulic valve-based active-heave compensation using a model-predictive controller with non-linear valve compensations, Ocean Engineering 152 (2018) 47–56.

[40] J. McPhee, R. A. Irani, On-line determination of a go-nogo state using a continous estimation of the system response (2018).

[41] S. Abujoub, J. McPhee, C. Westin, R. A. Irani, Unmanned aerial vehicle landing on maritime vessels using signal prediction of the ship motion (2018) 1–9.

[42] J. Ross, M. Seto, C. Johnston, Autonomous zero-visibility quadrotor landings towards persistent ship-based UAV ocean observations, OCEANS 2019 MTS/IEEE Seattle (2019) 1–6.

[43] J. S. Forrest, I. Owen, G. D. Padfield, S. J. Hodge, Ship-helicopter operating limits prediction using piloted flight simulation and time-accurate airwakes, Journal of Aircraft 49 (4) (2012) 1020–1031.

[44] K. McTaggart, ShipMo3D version 3.0 user manual for computing ship motions in the time and frequency domains (2012).

[45] S. Abujoub, Development of a landing period indicator and the use of signal prediction to improve landing methodologies of autonomous unmanned aerial vehicles on maritime vessels, MASc, Carleton University (2019).

[46] J. Brandt, M. Selig, Propeller performance data at low reynolds numbers, in: 49th AIAA Aerospace Sciences Meeting including the New Horizons Forum and Aerospace Exposition, 2011, p. 1255.

[47] I. Cheeseman, W. Bennett, The effect of ground on a helicopter rotor in forward flight (1955).

[48] R. Shevell, Fundamentals of Flight, Prentice Hall, 1989.

[49] A. Techet, Ocean waves, http://bit.ly/33fURdp, [Accessed: 7-May-2019] (2005).

[50] U. Military, Military specification MIL-F-8785C (1980).

[51] P. Janssen, The Interaction of Ocean Waves and Wind, Cambridge, 2004. doi:10.1017/CBO9780511525018.